

Neutron Stars as Sources of High Energy Particles – the case of RPP *

Bronisław Rudak

CAMK, Rabiańska 8, Toruń, Poland
also TCFA NCU, Toruń, Poland

Abstract. Highly magnetised rapidly spinning neutron stars are widely considered to be natural sites for acceleration of charged particles. Powerful acceleration mechanism due to unipolar induction is thought to operate in the magnetospheres of isolated neutron stars, bringing the particles to ultrarelativistic energies at the expense of the neutron star rotational energy, with inevitable emission of high energy photons.

The aim of this review is to present basic ingredients of modern models of magnetospheric activity of rotation powered pulsars in the context of high-energy radiation from these objects. Several aspects of pulsar activity are addressed and related to spectacular results of pulsar observations with two major satellite missions of the past – CGRO and ROSAT. It is then argued that high sensitivity experiments of the future - GLAST, VERITAS and MAGIC - will be vital for a progress in our understanding of pulsar magnetospheric processes.

In a conservative approach rotation powered pulsars are not expected to be the sources of UHE Cosmic Rays. However, several scenarios have been proposed recently to explain the UHECR events above the GZK limit with the help of acceleration processes in the immediate surrounding of newly born pulsars. Major features of these scenarios are reviewed along with references to contemporary models of magnetospheric activity.

1 Introduction

High energy radiation from various classes of galactic and extragalactic objects has been observed for nearly 30 years. Large fraction of the galactic sources are associated with neutron stars: rotation powered pulsars (RPP), accretion powered pulsars (APP), cooling neutron stars, and soft gamma-ray repeaters (SGR). Rotation powered pulsars like Crab, Vela and Geminga have a long history of successful observations with balloon-born and satellite gamma-ray and X-ray experiments. Performance of old experiments had been, however, surpassed in terms of sensitivity, energy range, number of positive detections, or photon statistics per object by the COMPTON Gamma-Ray Observatory (CGRO) and Röntgen Satellit (ROSAT). Spectacular re-

* Invited Review at International School “Physics and Astrophysics of Ultra High Energy Cosmic Rays”, June 2000, Paris-Meudon (France), to be published in Lecture Notes in Physics (Springer)

sults of observational campaigns of RPP with ROSAT and CGRO induced a new wave of interest in theoretical aspects of pulsar magnetospheric activity.

Pair creation paradigm is a pivotal element in any model of magnetospheric activity of RPP. Electron-positron pairs (e^\pm -pairs) are necessary since they are thought to be responsible for radio emission observed in radiopulsars and interpreted as the coherent curvature radiation of e^\pm plasma. Pairs can be produced in magnetospheric environments either via photon absorption in a dense field of soft photons (photon-photon collision) or via photon absorption in a strong magnetic field. In either case a supply of high-energy (HE) photons is required in order to fulfill stringent threshold conditions for the pair creation. It is quite reasonable then to assume that not all of those HE-photons would be subject to absorption. On the contrary, many HE photons will escape the magnetosphere without any attenuation. This argument leads us to expect that RPP (and all radiopulsars in particular) should be the sources of HE radiation. To make the production of HE photons possible, highly relativistic charged particles are to be injected into the magnetosphere. One may speculate that some of these particles will either retain their energy or regain it (under circumstances to be specified) upon escaping from the source. It is up to theoretical models of the RPP activity to show whether a rate of HE radiation and/or particles is interestingly high with respect to the sensitivity of recent and future HE detectors and telescopes.

This review focuses on RPP as sources of HE photons, presenting the most important observational results as well as their interpretation in terms of basic processes expected in the magnetospheres of RPP. The interpretation is offered by referring to a particular class of models of magnetospheric activity, known as polar gap models (or polar cap models). The name reflects the association of accelerator (the gap) with a polar cap on neutron star (NS) surface. Contrary to polar gap models, outer gap models [20] postulate the existence of accelerators located in regions where local corotation charge density reaches zero, close to the light cylinder. The e^\pm -pair creation occurs there either via one photon magnetic absorption (Crab-type outer gaps) or via photon-photon collisions (Vela type outer gaps). These models are relevant for both classical and millisecond pulsars with sufficiently high spin-down luminosity L_{sd} . The outer-gap accelerators cease to produce e^\pm pairs once the pulsar crosses the death-line $\log \dot{P} = 3.8 \log P - 11.2$ [18]. A modern version of the outer-gap accelerator, the so called ‘thick gap solution’ [19], is however able to accommodate pulsars of longer spin periods, like Geminga and B1055-52, removing at the same time serious problems with the original model of [20]. A detailed review of outer gap models in the context of HE radiation is available [19] and therefore we’ll concentrate on polar gap models.

The review is organised in the following way: Sect.2 defines basic quantities and introduces the assumptions used in pulsar physics. The status of X-ray and gamma-ray observations of RPP and essential features of the ra-

diation detected from several sources are presented in Sect.3. Sect.4 offers simple estimates of how effective a unipolar inductor (i.e. accelerator) can be when acting in the framework of a neutron star. Sect.5 discusses vertical structure of some polar gap accelerators. Sect.6 presents the properties of most important radiative processes induced by such inductors inside the RPP magnetosphere. With energetic arguments formulated in Sect.4, Sect.7 addresses a question of whether newly born and fastly spinning RPP might lead to generation of ultrarelativistic charged particles responsible then for the UHECR events observed above the GZK limit. Sect.8 emphasizes the anticipated role of high sensitivity HE/VHE missions of the near future in contributing to the physics of RPP.

2 Basic parameters

The aim of this section is to define basic quantities used throughout the review and to introduce their mutual relations. Several excellent monographs covering this subject in a detailed and sophisticated way are available e.g. [51] with a critical discussion.

The starting point are two major quantities measured for pulsars – period P , interpreted as a period of rotation of a neutron star, and \dot{P} , its time derivative. Suppose, that a neutron star of radius R_s and moment of inertia I rotates with angular velocity $\Omega = 2\pi/P$ which decreases in time (for whatever reason) at a rate $\dot{\Omega} = -2\pi P^{-2}\dot{P} < 0$. The rotational energy and its time derivative then read

$$E_{\text{rot}} = \frac{1}{2} I \Omega^2 \simeq 2 \times 10^{46} I_{45} P^{-2} \text{ erg} \quad (1)$$

$$\dot{E}_{\text{rot}} = I \Omega \dot{\Omega} \simeq -4 \times 10^{31} I_{45} \dot{P}_{-15} P^{-3} \text{ erg s}^{-1} \quad (2)$$

where P is in seconds, $\dot{P}_{-15} \equiv \dot{P}/10^{-15}$ and $I_{45} \equiv I/10^{45} \text{ g cm}^2$. Instead of \dot{E}_{rot} one uses the so called spin-down luminosity L_{sd} defined as

$$L_{\text{sd}} \equiv -\dot{E}_{\text{rot}}. \quad (3)$$

The name *luminosity* is misleading since the carriers of the major part of \dot{E}_{rot} are not luminous for us: no one has ever managed to “see” them in a direct way by any type of detector (but see Sect.7) and their nature is model-dependent, at least for the time being. Therefore we need a model for the spin-down of a neutron star. Let us assume that a magnetic dipole is attached to the center of a neutron star, with its moment inclined at angle α to the spin axis $\boldsymbol{\Omega}$, and let the mean strength of the field at the stellar surface is B_s . The magnetic dipole, rotating in a vacuum will emit energy at the rate

$$L_{\text{magn}} = \frac{2}{3c^3} B_s^2 \sin^2 \alpha R_s^6 \Omega^4 \quad (4)$$

suggesting thus the following model of the neutron star spin-down:

$$L_{\text{sd}} = L_{\text{magn}}. \quad (5)$$

The quantity $B_s \sin \alpha$ can be inferred from P and \dot{P} for a neutron star with known values of I and R_s . For a large number of randomly oriented rotators the factor $\sin^2 \alpha$ can be replaced with its averaged value of $2/3$.

Another model, where the dipolar radiation is replaced with a magnetospheric wind of particles [34], gives similar result as (4) for an orthogonal rotator:

$$L_{\text{sd}} = L_{\text{wind}} \approx \frac{1}{c^3} B_s^2 R_s^6 \Omega^4 \quad (6)$$

and therefore is independent of the angle α . Since there exists no observational support for \dot{P} depending on $\sin \alpha$ the standard approach is to apply the latter model to derive the strength of dipolar component of the magnetic field

$$B_{12}^2 = 10^{15} I_{45} R_6^{-6} P \dot{P} \quad (7)$$

where $B_{12} \equiv B_s/10^{12}\text{G}$, and $R_6 \equiv R_s/10^6\text{cm}$.

Assuming that B_s does not change with time one can integrate (7) to obtain the characteristic spin-down time scale τ – a period of time elapsed since the pulsar was born with initial period P_i

$$\tau = \frac{P}{2\dot{P}} \left[1 - \frac{P_i^2}{P^2} \right] \text{ s}. \quad (8)$$

As long as $P_i \ll P$, which is thought to be satisfied for all classical pulsars and most of millisecond pulsars, the last factor in (8) plays no role and thus $\tau \approx P/2\dot{P}$.

It is likely that neutron star magnetic fields contain high-order multipoles which may dominate the dipolar component at the surface level. Their relative amplitudes as well as distribution remain, however, unknown. It will be assumed throughout the paper that the dipolar magnetic field is not distorted by rotational effects or presence of strong outflowing wind of particles (the latter effect has been recently invoked to decrease very high values of B_s inferred from P and \dot{P} for two SGRs [39]; in consequence, their classification as magnetars became questionable). The field is therefore approximated with axisymmetric static dipole with field lines satisfying $r \sin^{-2} \theta = R_{\text{dc}}$ in polar coordinates r and θ , with the dipole constant R_{dc} . The dipole constant at which rigid rotation reaches speed-of-light limit is called the light cylinder: $R_{\text{lc}} = c/\Omega$. All field lines which cross the light cylinder are then considered as open lines, and their footpoints on the stellar surface define two polar caps of radius $R_{\text{pc}} \approx R_s \cdot (R_s/R_{\text{lc}})^{1/2}$, where the latter factor is the sine function of the polar coordinate θ for the outer rim of the polar cap: $\sin \theta_{\text{pc}} = (R_s/R_{\text{lc}})^{1/2}$.

3 Observational overview of high energy domain

A posteriori evidence that high-energy activity of pulsars must somehow draw from their rotational energy $E_{\text{rot}} = I\Omega^2/2$ comes from a simple finding that, essentially, the success of detection of a particular pulsar in X-rays and/or gamma-rays was strongly correlated with its position in the lists of targets ranked by spin-down flux values L_{sd}/D^2 .

The aim of this section is to review recent observational status of RPP in the high-energy (HE) domain, with X-rays included. The HE domain is hereafter arbitrarily defined as extending from a fraction of keV up to about 30 GeV. Nevertheless, more emphasis is put on gamma-ray results. Gamma-ray detections are particularly precious since their interpretation is thought to be less ambiguous in comparison to X-ray detections. In the latter case (especially for very young objects) contributions from initial cooling, internal friction, or other factors of *a priori* unknown magnitude may dominate the X-ray emission (Note: indeed, four pulsars – Vela, Geminga, B1055-52 and B0656+14 – are classified as initial cooling candidates [7] since their X-ray emission is dominated by a component which may be modelled by a blackbody emission from a NS surface).

For more than 1500 pulsars known to date only about 35 positive detections in X-rays and no more than 9 detections in gamma-rays have been achieved. There are firm detections by CGRO of 7 pulsars (dubbed *Seven Samurai*) and another 2 cases classified as ‘likely’ detections. The gamma-ray sources were identified by virtue of flux pulsations with previously known P and \dot{P} . Crab and Vela are the only pulsars seen by all three instruments of CGRO. No trace of pulsed signal in VHE range (300 GeV – 30 TeV) has been found so far for the gamma-ray pulsars [80] [64] [81]. However, strong steady VHE emission is associated with 3 out of 9 gamma-ray pulsars. Two plerionic sources of the steady VHE radiation – The Crab Nebula and the plerion around B1706-44 – may serve as standard candles, with ‘grade A’ according to [81]. A third plerion – around the Vela pulsar – was given ‘grade B’ in the same ranking. All 9 gamma-ray pulsars are strong X-ray emitters.

The positions of these HE pulsars are shown in the $P - \dot{P}$ diagram of Fig.1 along with positions of about 700 radio pulsars for which \dot{P} values were available. A remarkable fact is that the location of X-ray sources does not correlate with the inferred strength of magnetic field B_s ; at least not in a naively anticipated way that high-B objects would emit HE radiation, whereas low-B objects would not. In particular, 10 millisecond pulsars – about thirty percent of all millisecond pulsars (the objects with $P \lesssim 0.01$ s and $\dot{P} \lesssim 10^{-17}$, i.e. with low B values: $B_s \lesssim 10^9$ G) known to date – have been detected as X-ray sources. So far, millisecond pulsars eluded the detection in gamma rays and just upper limits have been available for a handful of them from EGRET observations [53]. In the case of J0437-4715 the upper limit is interestingly tight – in disagreement with the empirical relation $L_\gamma \propto L_{\text{sd}}^{1/2}$

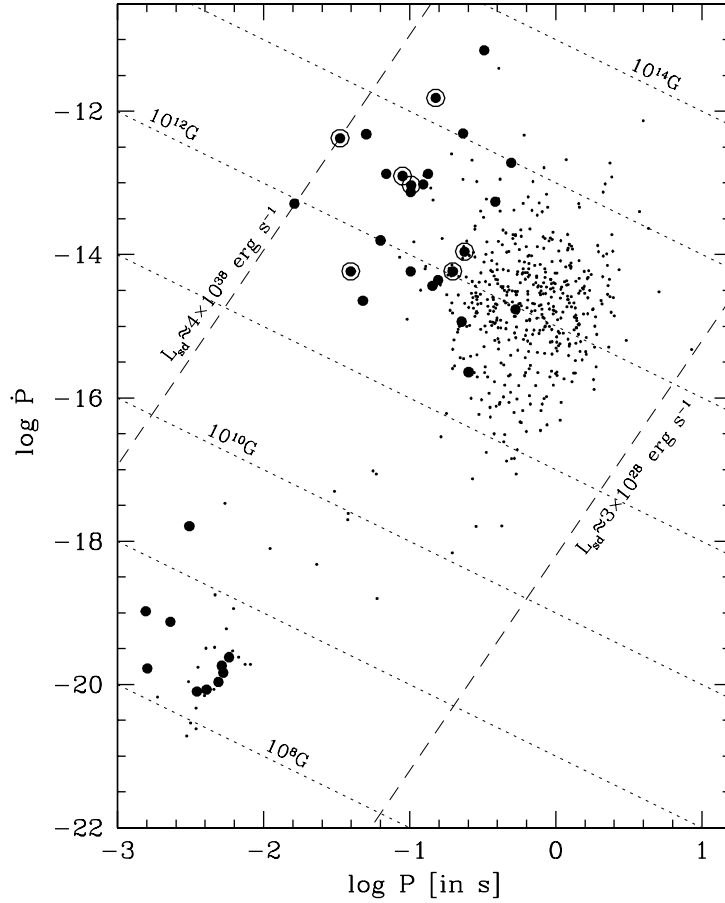


Fig. 1. $P - \dot{P}$ diagram for Rotation Powered Pulsars. The pulsars detected exclusively in radio are indicated with dots; they are taken mostly from the data base of [76]. Thirty five pulsars emitting X-rays are indicated with bullets. These include two objects recently discovered with RXTE: J0537-6910 in SNR N157B in LMC [49] is the fastest young pulsar known, spinning twice as fast as the Crab pulsar but with similar value of spin down luminosity; J1846-0258 in SNR Kes-75 [35], with $P = 0.32\text{s}$, the highest \dot{P} among all RPP and no radio counterpart so far. Seven bullets in circles indicate seven gamma-ray pulsars. Dashed lines correspond to constant values of the spin down luminosity L_{sd} . The upper line ($L_{\text{sd}} \approx 4 \times 10^{38} \text{erg s}^{-1}$) includes the Crab pulsar and J1846-0258, the lower one ($L_{\text{sd}} \approx 3 \times 10^{28} \text{erg s}^{-1}$) includes J2144-3933 – the slowest ($P = 8.5\text{s}$) radio pulsar detected so far [84]. Dotted lines correspond to constant values of the dipolar component of the surface magnetic field as inferred from P and \dot{P} .

(see Fig.3). Very recently, however, the likely detection of pulsed gamma-ray emission from J0218+4232 has been reported [47].

Spectral analysis for pulsars detected with ROSAT PSPC (0.1 keV to 2.4 keV) shows that in most cases a power-law spectral model provides acceptable fits to the data [7]. Moreover, an intriguing empirical relation between inferred X-ray luminosity and spin down luminosity was found, $L_X \approx 0.001 L_{sd}$, confirming rotational origin of most of the X-ray activity. An interesting point is that the relation was obtained for all the sources regardless their temporal characteristics (about 50 % of all pulsars detected with ROSAT are unpulsed sources). Fig.2 presents these results in a somewhat different way and for slightly different values for L_X (compiled by the author). A complementary empirical relation was found for pulsed emission from 19 pulsars observed with ASCA (0.6 keV to 10 keV). Assuming opening angle of X-rays to be one steradian, the inferred pulsed X-ray luminosity correlates with spin-down luminosity as

$$L_X = 10^{34} \left(\frac{L_{sd}}{10^{38} \text{ erg s}^{-1}} \right)^{3/2} \text{ erg s}^{-1}, \quad (9)$$

according to [63].

A similar power-law empirical relation holds for gamma-rays (cf. Fig.3), but with a different power-law index (e.g. [78]):

$$L_\gamma \simeq 10^{35} \left(\frac{L_{sd}}{10^{38} \text{ erg s}^{-1}} \right)^{1/2} \text{ erg s}^{-1}. \quad (10)$$

Important conclusion from Figs.2 and 3 is that neither L_X nor L_γ becomes a sizable fraction of L_{sd} . The most efficient conversion of spin-down luminosity into high-energy radiation is taking place for B1055-52 – the oldest pulsar among *Seven Samurai* – with $L_\gamma \simeq 0.1 L_{sd}$. Since in both, polar gap and outer gap models most of the energy gained by charged particles in the gaps is transferred to HE photons, it means that the wind of particles leaving the magnetosphere at the light cylinder is also unimportant energetically, i.e. $L_{wind} \ll L_{sd}$. Therefore, the lion's share of the spin down luminosity is probably carried away in a form of magnetic dipole radiation L_{magn} ; in terms of the so called magnetization parameter σ it means $\sigma \gg 1$ at the light cylinder (cf. Sect.7).

Broadband energy spectra per logarithmic energy bandwidth extending from radio, optical and UV, to X-rays and gamma-rays, constructed for pulsed phased-averaged components of *Seven Samurai* are particularly impressive [78] and instructive. Fig.4 reveals substantial spectral differences among the objects, which became a subject of theoretical debates and speculations.

Short spectral characteristics of all 9 gamma-ray pulsars (including 2 'likely' sources) are given below after [78] for EGRET, [68] for COMPTEL and [69] for OSSE (and references therein). These instruments operating on board CGRO [43] covered the following parts of HE domain: the Oriented

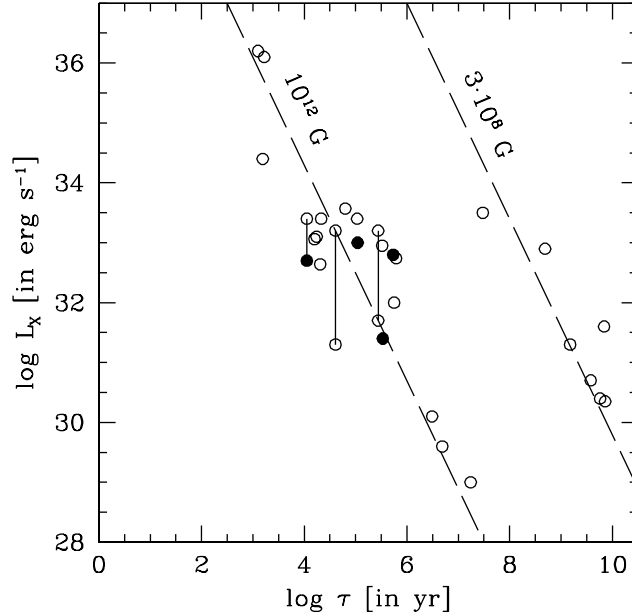


Fig. 2. X-ray luminosity versus spin-down age τ for 29 out of 35 pulsars detected with ROSAT, ASCA and RXTE. Isotropic emission into 4π steradians was assumed for pulsed and unpulsed sources to infer L_X . The empirical relation $L_X \approx 0.001 L_{sd}$ found by [7] can be rewritten as $L_X \propto B_s^{-2} \tau^{-2}$. If all classical and millisecond pulsars were to have the surface magnetic field B_s of a fixed value 10^{12}G and $3 \times 10^8\text{G}$, respectively, they would follow the two dashed lines labelled with B_s . Four filled circles are the initial cooling candidates; in increasing τ these are: B0833-45 (Vela) [55], B0656+14 [59], J0633+17 (Geminga) [37], and B1055-52 [66]. In three cases the fitting of the data with either blackbody or power law spectral model was equally justified, but inferred X-ray luminosities are strongly model-dependent (circles connected with vertical bars); in increasing τ these objects are: B0833-45 [55], B2334+61, and B0114+58 [67].

Scintillation Spectrometer Experiment (OSSE) was operating in the energy range 50 keV – 10 MeV, the Imaging Compton Telescope (COMPTEL) – in the energy range 0.75 MeV – 30 MeV, and the Energetic Gamma Ray Experiment Telescope (EGRET) in the energy range 50 MeV – 30 GeV.

1) B0531+21 (Crab) – Detected by EGRET, COMPTEL, and OSSE. Its gamma-ray flux consists of pulsed and unpulsed components, the latter one coming from Crab Nebula. The overall phase-averaged photon spectrum in the range between 50 keV and 10 GeV is described satisfactorily by a broken

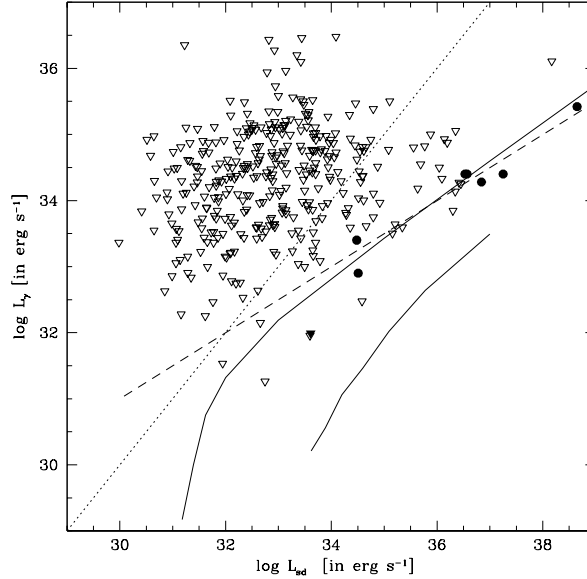


Fig. 3. Gamma-ray luminosity versus spin-down luminosity for seven pulsars (filled dots) detected with the CGRO instruments. Opening angle of one steradian was assumed for the gamma-ray emission. Open triangles are the EGRET upper limits after [53] for 350 objects, including seven millisecond pulsars. The filled triangle indicates the upper limit for J0437-4715 [33]. Note, that most of the upper limits are well above the maximum possible value for L_γ set by $L_\gamma = L_{sd}$ (dotted line). The dashed line marks the empirical relation derived for the CGRO pulsars: $L_\gamma \propto L_{sd}^{1.2}$. Solid lines show evolutionary tracks for a classical pulsar with $B_s = 10^{12}$ G (upper line) and a millisecond pulsar with $B_s = 10^9$ G (lower line) according to the phenomenological model of [61].

power-law shape $dN_\gamma/d\varepsilon \propto \varepsilon^{-\alpha}$ with a break at $\varepsilon_{br} \simeq 120$ keV, and photon power-law index $\alpha = 1.71$ for $\varepsilon \leq \varepsilon_{br}$, and $\alpha = 2.21$ for $\varepsilon > \varepsilon_{br}$. The energy flux is $f_\gamma \approx 7.3 \times 10^{-9} \text{ erg s}^{-1} \text{ cm}^{-2}$.

2) B1509-58 – Detected by COMPTEL and OSSE. The initial COMPTEL detection was of marginal significance ($\sim 3\sigma$ -detection) in a narrow (0.75 – 1 MeV) energy band. However, recent analysis shows that the spectrum extends to higher energies with a cutoff around 10 MeV [46] (Note: this new finding is not marked in Fig.4). The energy flux at 1 MeV may be as high as $1.4 \times 10^{-9} \text{ erg s}^{-1} \text{ cm}^{-2}$, but the COMPTEL point stands above the corresponding OSSE point by a factor of 4. The OSSE spectral fit between 50 keV and ~ 5 MeV with $dN_\gamma/d\varepsilon \propto \varepsilon^{-1.68}$ yields $f_\gamma \approx 5.6 \times 10^{-10} \text{ erg s}^{-1} \text{ cm}^{-2}$. EGRET put strong upper limits for photon flux above 100 MeV and 1 GeV ,

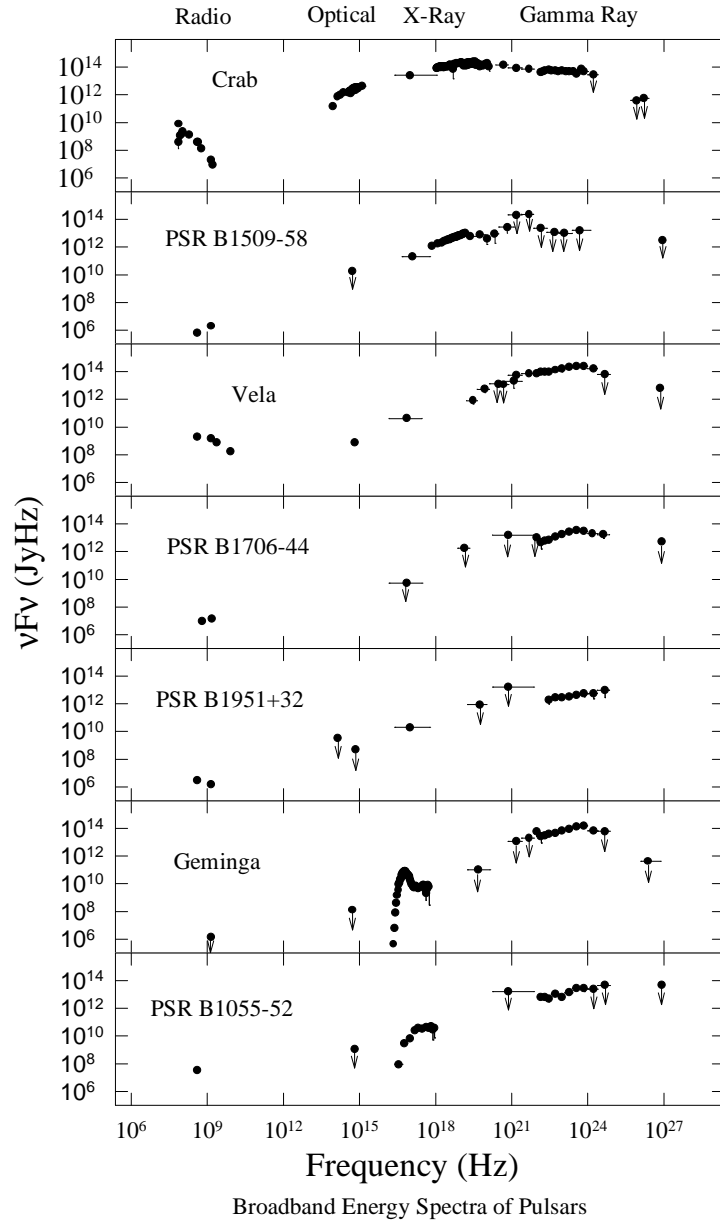


Fig. 4. Phase-averaged spectra for seven gamma-ray pulsars (Courtesy D.J. Thompson).

which clearly fall below simple power-law extrapolation of the OSSE spectral fit. That indicates a presence of spectral roll-over at several MeV, in agreement with the cutoff claimed by [46]. The pulsar has the highest inferred magnetic field ($B_s \simeq 1.5 \times 10^{13} \text{G}$) among seven gamma-ray pulsars, an essential point for explaining the cutoff at 10 MeV as due to photon-splitting effect [38].

3) B0833-45 (Vela) – Detected by EGRET, COMPTEL, and OSSE. Its phase-averaged photon spectrum between 30 MeV and 2 GeV can be reproduced as a power law with $\alpha = 1.7$, and a strong spectral break above ~ 4 GeV. The spectrum flattens out in the OSSE range with $\alpha = 1.3$. Estimated energy flux reaches $\sim 9 \times 10^{-9} \text{ erg s}^{-1} \text{ cm}^{-2}$ (the brightest object in the gamma-ray sky).

4) B1706-44 – Young Vela-like pulsar, detected by EGRET. The spectrum extends from 50 MeV beyond 10 GeV and may be approximated with a broken power law, with photon index α changing from 1.27 to 2.25 at 1 GeV.

5) B1951+32 – Detected by EGRET and COMPTEL. The spectrum extends from 0.75 MeV up to 30 GeV and may be approximated with a single power law with photon index $\alpha = 1.89$. Extremely sharp cut-off, with no apparent decline in the flux level. But extrapolation towards TeV falls 2 order of magnitude above an upper limit (not shown in Fig.4) set by Whipple group.

6) J0633+17 (Geminga) – Confirmed detection by EGRET only. The photon spectrum may be approximated with a single power law, with $\alpha = 1.50$, extending from 30 MeV to a roll-off at 2 GeV.

7) B1055-52 – Detected by EGRET above 70 MeV. Its spectrum can be represented by a single power law with photon index $\alpha = 1.73$, and a possible break around 1 GeV.

8) B0656+14 – A 3σ -detection by EGRET had been reported. The pulsar with its parameters (P , \dot{P} , and particularly L_{sd}) resembles Geminga nad B1055-52. Its photon spectrum estimated for low number of events may be represented between 10 MeV and 10 GeV as a very steep power-law with the index $\alpha = 2.8$.

9) J0218+4232 – Marginal detection by EGRET (at 3.5σ level) of pulsed emission has been reported recently in the energy range 100 MeV – 300 MeV for this distant ($D \gtrsim 5.85 \text{ kpc}$) millisecond ($P = 0.0023 \text{ s}$) pulsar in a binary system with a low-mass white dwarf [47]. The inferred luminosity of the pulsed emission for 1 steradian opening angle reaches $L_\gamma \simeq 1.64 \times 10^{34} \text{ erg s}^{-1} \simeq 0.07 L_{\text{sd}}$.

Gamma-ray light curves differ significantly from those in X-rays, optical, and radio. Their most striking feature are relatively long duty cycles as well as phase shifts in comparison to the radio pulses. Only for the Crab pulsar the peaks in gamma-rays as well as in radio wavelengths occur at the same rotational phases. The light-curve shapes fall into two categories. The Crab pulsar, Vela and Geminga show two sharp pulses separated in phase by

0.4 – 0.5 and connected by an interpulse bridge of considerable level. B1706-44 shows two peaks separated by 0.2 in phase, with some hints of a third component in between. Other pulsars exhibit broad single pulses. Unknown opening angles for gamma-ray emission introduce a factor of uncertainty when inferring the gamma-ray luminosities. Broad peaks in gamma-ray pulses do not necessarily mean large opening angles for gamma-ray emission. Polar cap models, which rely on purely dipolar magnetic fields postulate nearly aligned rotators, where inclination of magnetic axis to spin axis is comparable to the angular extent of the polar cap [27].

With a discovery of sharply peaked pulsed X-ray emission in the fastest millisecond pulsar B1937+21 an apparently separate group of millisecond X-ray pulsars emerges, with its members – B1821-24 [63], J0218+4232 [47], and B1937+21 [75] – being scaled-down versions of the Crab pulsar as far as sharp pulse profiles and hard power-law X-ray spectra are concerned. An astonishing common feature within the group is the same strength of the magnetic field estimated at the light cylinder and the fact that it matches the strength of the Crab pulsar magnetic field at the light cylinder.

4 Unipolar induction – a toy model

4.1 Vacuum rotator

Let us begin with a frequently invoked order-of-magnitude estimate advertising rotating neutron stars as potentially powerful accelerators and thus good candidates to explain UHECR (the problem addressed in Sect.7). Consider a neutron star of radius R_s and surface magnetic field B_s as a perfect conductor. For the rotating star with its dipolar magnetic field immersed in a vacuum an external quadrupole electric field \mathcal{E} develops, with non-zero component along magnetic field lines at the surface. The corresponding electrostatic potential Φ in polar coordinates r and θ reads [51]

$$\Phi(r, \theta) = -\frac{Q}{r} (3 \cos^2 \theta - 1), \quad (11)$$

where $Q \propto B_s/P$ is the quadrupole moment. Maximal electromotive force will then be induced between one of the two poles of the star and its equator:

$$\Delta\Phi_{\text{equator}} = \frac{1}{2c} B \Omega R_s^2. \quad (12)$$

The corresponding voltage drop

$$\Delta V_{\text{equator}} \approx 3 \times 10^{16} B_{12} R_6^2 P^{-1} \text{Volt} \quad (13)$$

reaches huge values. If such a unipolar inductor was to operate in the Crab pulsar, B1509 or J1846-0258 (see Fig.1), it would bring a fully ionized atom of

iron ($Z = 26$) close to the energy of 10^{20} eV. However, the assumption about a vacuum surrounding the entire star is not correct. The space containing field lines closed within the light cylinder is expected to fill in quickly with trapped charged particles supporting the electric field which forces them to corotate with the star (cf. the subsection below). Therefore, the only regions on the stellar surface appropriate for the unipolar induction to act are those containing open field lines only, i.e. the polar caps. From (11) and (12) the potential difference between the pole and the outer rim of the polar cap follows as

$$\Delta\Phi_{\text{pc}} = \Delta\Phi_{\text{equator}} \left(\frac{R_{\text{pc}}}{R_{\text{s}}} \right)^2, \quad (14)$$

with voltage drop of

$$\Delta V_{\text{pc}} \approx 7 \times 10^{12} B_{12} P^{-2} \text{ Volt}. \quad (15)$$

4.2 Rotating magnetosphere

We will concentrate hereafter on a class of models where the supply of charged particles from a neutron star surface along open field lines is not limited by binding or cohesive energy of the particles and therefore can reach the so-called Goldreich–Julian rate at the surface. Such a supply of charges was dubbed ‘Space Charge Limited Flow’ [74], [4] or ‘free emission’. A concise but to-the-point account of essential properties of the SCLF models has been presented recently by [5].

Three boundary conditions essential for the electrodynamics above the polar cap are [52]:

- 1) $\mathcal{E} \cdot \mathbf{B} = 0$ for the magnetosphere within the closed field lines,
- 2) $\Phi = 0$ at the surface and at the interface between the closed magnetosphere and the open field lines,
- 3) $\mathcal{E}_{\parallel} = 0$ at the surface level.

Last but not least, it is assumed that the outflow is stationary and the magnetosphere remains axisymmetric.

The electric field \mathcal{E} required to bring a charged particle into corotation is

$$\mathcal{E} + \frac{1}{c} ((\boldsymbol{\Omega} - \boldsymbol{\omega}_{\text{LT}}) \times \mathbf{r}) \times \mathbf{B} = 0 \quad (16)$$

where the inertial-frame dragging effect is included [52] with $\boldsymbol{\omega}_{\text{LT}} = \kappa_{\text{g}}(R_{\text{s}}/r)^3 \boldsymbol{\Omega}$, and $\kappa_{\text{g}} = 2GI/R_{\text{s}}^3 c^2$.

Charge density necessary to support this local \mathcal{E} is

$$\rho_{\text{corot}} = \frac{1}{4\pi} \nabla \cdot \mathcal{E} \approx -\frac{\boldsymbol{\Omega} \cdot \mathbf{B}}{2\pi c} \left[1 - \kappa_{\text{g}} \left(\frac{R_{\text{s}}}{r} \right)^3 \right] \quad (17)$$

The charge density ϱ_{corot} due to SCLF at $r = R_s$ is called Goldreich–Julian charge density and it is labelled with ‘GJ’:

$$\varrho_{GJ} \approx -\frac{\boldsymbol{\Omega} \cdot \mathbf{B}}{2\pi c} [1 - \kappa_g]. \quad (18)$$

As charged particles flow out along the open field lines a deviation of the local charge density ϱ_{local} from the local corotation density ϱ_{corot} develops. By using now two relations satisfied in the dipolar structure, $B(r) \propto r^{-3}$ and $\varrho(r) \propto r^{-3}$, one obtains a simple formula for local deviation from the corotation charge density:

$$\varrho_{local} - \varrho_{corot} = \frac{\boldsymbol{\Omega} \cdot \mathbf{B}}{2\pi c} \kappa_g \left[1 - \left(\frac{R_s}{r} \right)^3 \right]. \quad (19)$$

Accordingly, the accelerating potential drop in SCLF reads

$$\Delta\Phi_{\parallel} \approx \Delta\Phi_{pc} \kappa_g \left[1 - \left(\frac{R_s}{r} \right)^3 \right]. \quad (20)$$

This is a remarkable result obtained by [52]: due to the inertial-frame dragging effect the particles drop through the potential which is significantly larger than in the classical approach of [4] (for $P = 1$ s it becomes 10 times larger). Moreover, the electric field \mathcal{E}_{\parallel} develops now along all open lines regardless their orientation with respect to the spin axis (the effect is not shown in this simplified presentation). Therefore, all open field lines are ‘favourable’, in contrast to [4].

5 Electric field structure in SCLF gaps

The model with frame dragging effects [52], presented in a simplified form in subsection 4.2, does not take into account possible feed-back effect due to e^{\pm} -pairs formed via photon absorption within open magnetic field lines. Copious pair formation occurs in a relatively thin layer called for this reason a pair formation front (PFF). The creation of pairs leads to screening of the accelerating field \mathcal{E}_{\parallel} within the layer of PFF. A detailed picture of this effect would require to follow the dynamics of electrons and positrons in a self-consistent way. Instead, it is reasonable to assume, that the field is shorted out at the height where the first e^{\pm} -pair is created (hereafter denoted as h_c): $\mathcal{E}_{\parallel} = 0$ for $h \geq h_c$.

The problem of electric field structure in the context of SCLF with boundary condition $\mathcal{E}_{\parallel} = 0$ set at $h_0 = 0$ (stellar surface) and at $h \geq h_c$ (PFF) was formulated and solved by [40]. The solution is rather lengthy and includes special functions. It is however possible to obtain simple but quite accurate analytical approximations. As long as the length h_c of the accelerator is of

the order of polar cap radius R_{pc} , the accelerating electric field may be approximated according to [29] as

$$\mathcal{E}_{\parallel} \approx -1.46 \frac{B_{12}}{P^{3/2}} h \left(1 - \frac{h}{h_c}\right) f_1(\xi) \cos \chi \text{ Gauss}, \quad (21)$$

where $B_{12} = B_s/10^{12}\text{G}$, P is the spin period in seconds, χ is the angle between the spin axis and the magnetic moment of the rotating star, h is expressed in cm, and $M = 1.4 M_{\odot}$, $R_s = 10^6\text{cm}$. The magnetic colatitude $\xi \equiv \theta/\theta(\eta)$ is scaled with the half-opening angle of the polar magnetic flux tube $\theta(\eta)$, where $\eta \equiv 1 + h/R_s$. The magnetic colatitude function $f_1(\xi)$ is a monotonically decreasing function, with $f_1(0) \simeq 1$ and $f_1(1) = 0$.

Vertical structure of the electric field depends (via the location of PFF) on radiative processes which induce the pair creation: curvature radiation and inverse Compton scattering on soft X-ray photons from the stellar surface (brief characteristics of these processes is presented in the next section). An interesting effect was noticed in this context [40]: Suppose that a small fraction of positrons is stopped by a residual (non-zero) electric field at the site of their creation and then forced to flow towards the stellar surface (the effect noticed already by [74]). The backflowing positrons are expected to induce a formation of an additional PFF, which would short out the electric field at h_0 . These positrons cool upon the action of ICS and CR. With reasonable surface temperatures ($T_s \sim 5 \times 10^5\text{K}$) it is ICS which dominates the cooling of upward moving electrons and downward moving positrons. Therefore, the e^{\pm} -pair creation will be induced by upscattered photons from the stellar surface, rather than by curvature photons. The situation is not symmetrical, however, for electrons and positrons since the field of soft photons is not symmetrical with respect to both types of particles. In consequence, the positrons cool more efficiently, the ICS-induced cascades are easier to achieve for positrons than electrons and thus a lower PFF (where $\mathcal{E}_{\parallel} = 0$) tends to be located above the stellar surface. Such a situation is not stable, therefore. However, elevating the accelerator up to altitude $h_0 \sim 1 R_s$ above the surface diminishes the role of the ICS; the CR cooling dominates here and a stable accelerator is possible. No self-consistent calculations of such a ‘sandwich-like’ accelerator exist at present, but the results obtained by [40] with an approximate treatment of the problem look promising indeed.

6 Radiative processes in pulsar magnetospheres

Cooling of ultrarelativistic electrons via curvature radiation (CR) and magnetic inverse Compton scattering (ICS) are the most natural ways of producing hard gamma-rays capable of inducing cascades of e^{\pm} -pairs and secondary HE photons. These two processes dominate within two distinct ranges of Lorentz factors γ of primary electrons.

When $\gamma \lesssim 10^6$, magnetic inverse Compton scattering plays a dominant role in braking the electrons and it is the main source of hard gamma-ray photons [73]. Energy losses due to resonant ICS limit the Lorentz factors of the particles to a level which depends on electric field strength \mathcal{E}_{\parallel} , temperature T and size of hot polar cap, and magnetic field strength B_s [83][72]. The Lorentz factors can then be limited even to $\sim 10^3$. This stopping effect becomes more efficient for stronger magnetic fields, and it was suggested as an explanation for the observed cutoff at ~ 10 MeV in the spectrum of B1509-58 [72].

However, in their modern versions the accelerators of particles are strong enough to overpower the ICS cooling. In consequence, very high Lorentz factors – $\gamma \gtrsim 10^6$ – are achieved by electrons, limited by CR. The first detailed scenario of radiative processes in CR-induced cascades was presented by [23] and despite many modifications and additions its basic features remain valid. The model assumes that primary electrons accelerated to ultrarelativistic energies emit curvature photons which in turn are absorbed by the magnetic field and e^{\pm} -pairs are created. These pairs cool off instantly via synchrotron radiation process. Whenever the SR photons are energetic enough they may lead to further creation of pairs, etc.. ICS can still be incorporated to the models with CR-induced cascades as the process relevant for e^{\pm} -pairs, since typical Lorentz factors of theirs do not exceed $\sim 10^3$. According to the analytical model of [85] the empirical relations for X-ray and gamma-ray luminosities of pulsars (presented in Sect.3) can be reproduced satisfactorily when the ICS involving e^{\pm} -pairs is included.

Processes relevant for production and transfer of HE radiation in pulsar magnetospheres are, therefore:

- Curvature Radiation,
- Magnetic Inverse Compton Scattering,
- Magnetic Pair Creation $\gamma \rightarrow e^{\pm}$
- Synchrotron Radiation,
- Photon splitting $\gamma \rightarrow \gamma + \gamma$,
- Photon-photon Pair Creation $\gamma + \gamma \rightarrow e^{\pm}$.

Basic properties of these processes are briefly reviewed below. The last process in the list has been omitted. The reason is that, whenever recalled in the context of pulsar magnetospheres, photon-photon pair creation is treated exactly as in free space. Such treatment is justified in models of ‘thick outer gaps’ [19] but within the framework of polar cap models this is not the case, in general. However, no handy formula is available for the cross section of this process in the limit of high B and standard non-magnetic formulae are in use whenever necessary.

In order to illustrate the significance of these processes in forming HE spectrum extending over many decades in energy, the numerically calculated effects due to the first 4 processes in the list will be presented in Fig.5 (after [30]) along with overlaid data points for the Vela pulsar. The dipolar field

in the Vela pulsar does not exceed 10^{13}G and thus photon splitting is not competitive to magnetic pair creation; its effects are negligible and will not be shown. The electric field structure of the accelerator used in these calculations is taken after [40] and appropriate rescaling due to $h_0 > 0$. However, the case calculated for Fig.5 was chosen with $h_0 = 3R_s$, i.e. much higher than in [40], in order to better reproduce the phase averaged spectrum of the Vela pulsar.

6.1 Curvature radiation

Relativistic electron of energy γmc^2 (we take $\gamma \gg 1$) sliding along the magnetic field line of curvature ϱ_{cr} will emit photons with a continuum energy spectrum peaked at

$$\varepsilon_{\text{peak}} \approx 0.29 \varepsilon_{\text{cr}}, \quad (22)$$

where

$$\varepsilon_{\text{cr}} = \frac{3}{2} c \hbar \frac{\gamma^3}{\varrho_{\text{cr}}}, \quad (23)$$

is called the characteristic energy of CR. The radius ϱ_{cr} for a purely dipolar line attached to the outer rim of the polar cap can be approximated not far away from the NS surface as $\varrho_{\text{cr}} \approx \sqrt{R_s \cdot R_{\text{lc}}} \approx 10^8 \sqrt{P} \text{cm}$. The cooling rate of that electron is

$$\dot{\gamma}_{\text{cr}} = -\frac{2}{3} \frac{e^2}{mc} \frac{\gamma^4}{\varrho_{\text{cr}}^2}. \quad (24)$$

For a monoenergetic injection function of electrons $Q(\gamma) \propto \delta(\gamma - \gamma_0)$ and their cooling due solely to CR the electrons will assume a single power-law distribution in energy space $N_\gamma(\text{el.}) \propto \gamma^{-4}$ for $\gamma < \gamma_0$ as long as they stay within the region of the cooling. Their escape introduces a natural low-energy cutoff γ_{cutoff} in $N_\gamma(\text{el.})$. Therefore, the unabsorbed CR energy spectrum $f_\varepsilon(\varepsilon)$ due to the injected electrons has a broken power-law shape, with a high-energy limit set by γ_0 and the break at some energy $\varepsilon_{\text{break}}$. For $\varepsilon > \varepsilon_{\text{break}}$ the energy spectrum is $f_\varepsilon(\varepsilon) \propto \varepsilon^{-2/3}$, and $f_\varepsilon(\varepsilon) \propto \varepsilon^{+1/3}$ for $\varepsilon < \varepsilon_{\text{break}}$. Since nonthermal spectra cover usually many decades in energy it is more convenient to use $\varepsilon f_\varepsilon(\varepsilon)$ for easy comparison of power in different parts of energy space (see Figs.4 and 5). Accordingly, $\varepsilon f_\varepsilon(\varepsilon) \propto \varepsilon^{+1/3}$ above the break, and $\propto \varepsilon^{+4/3}$ below the break.

The cutoff limit γ_{cutoff} can be found by comparing the characteristic cooling time scale $t_{\text{cr}} \equiv \gamma/|\dot{\gamma}_{\text{cr}}|$ with the estimated time of escape t_{esc} , which we take as $t_{\text{esc}} \approx \varrho_{\text{cr}}/c$. Therefore

$$\varepsilon_{\text{break}} \approx 0.29 \cdot \frac{9}{4} \hbar \frac{c}{r_0} \approx 44 \text{ MeV}, \quad (25)$$

where r_0 is the classical electron radius. Note, that the photon energy $\varepsilon_{\text{break}}$ at which the spectral break occurs does not depend on any pulsar parameters.

The spectrum of CR calculated numerically to model the Vela pulsar [30] is shown in Fig.5 as dot-dashed line. High-energy cutoff due to one-photon

magnetic absorption occurs around 10 GeV. Note the importance of gamma-ray detectors capable to operate above 10 GeV for (in)validating the model. The low-energy CR spectral break $\varepsilon_{\text{break}}$ is prominent at ~ 40 MeV. Below $\varepsilon_{\text{break}}$ the power of CR decreases and eventually becomes unimportant at ~ 1 MeV where the synchrotron component takes over.

6.2 Magnetic pair creation

Pair creation via magnetic photon absorption ($\gamma + \mathbf{B} \rightarrow e^\pm + \mathbf{B}$) is kinematically correct since the magnetic field can absorb momentum. To ensure high chances for the process to occur it is not enough for a photon propagating at some angle α to local \mathbf{B} to satisfy the energy threshold condition, $\sin \psi \cdot \varepsilon \geq 2mc^2$, but high optical thickness $\tau_{\gamma B}$ within the magnetosphere is required. In fact the condition $\tau_{\gamma B} = 1$ has been used as a criterium for the so called death-line for radiopulsars in the $P - \dot{P}$ diagram. Maximal values of $\sin \psi$ for curvature photons in the dipolar field do not exceed $\sim 0.1 \sin \theta_{\text{pc}} \approx 0.0014 P^{-1/2}$ [74], so the both conditions are difficult to meet for long-period rotators.

The absorption coefficient for the process as described in [32] and used to calculate $\tau_{\gamma B}$ reads

$$\eta(\varepsilon) = \frac{1}{2} \frac{\alpha}{\lambda_c} \frac{B_\perp}{B_{\text{crit}}} T(\chi) \quad (26)$$

where α is a fine structure constant, λ_c is a Compton wavelength, $B_{\text{crit}} = m^2 c^3 / e \hbar \simeq 4.4 \times 10^{13} \text{G}$, B_\perp is the component of the magnetic field perpendicular to the photon momentum, and $\chi \equiv \frac{1}{2} \frac{B_\perp}{B_{\text{crit}}} \frac{\varepsilon}{m_e c^2}$ is the Erber parameter χ . The function $T(\chi)$ is then approximated as $T(\chi) \approx 0.46 \exp(-4f/3\chi)$, which is valid for $\chi \lesssim 0.2$; for $\chi \gtrsim 0.2$ this approximation starts to overestimate η . The function f is the near-threshold correction introduced by [24] important in particular in the case of classical pulsars. Electron-positron pairs created through the magnetic absorption radiate then via the synchrotron process (SR) described below.

6.3 Synchrotron radiation

Consider a particle of energy γmc^2 gyrating around a local field line at a pitch angle ψ . Let γ_\parallel denotes the Lorentz factor of the reference frame comoving with the center of the gyration. As long as $\gamma_\parallel \gg 1$ it relates to the pitch angle ψ via $\sin \psi \approx \gamma_\parallel^{-1}$. The energy available for synchrotron emission at the expense of the particle is $\gamma_\perp mc^2$, and $\gamma = \gamma_\perp \gamma_\parallel$.

The rate of SR cooling reads

$$\dot{\gamma}_{\text{sr}} = -\frac{2}{3} \frac{r_0^2}{m_e c} B^2 \gamma_\perp^2 = -\frac{2}{3} \frac{r_0^2}{m_e c} B^2 \sin^2 \psi \gamma^2. \quad (27)$$

In comparison to the CR cooling it is enormous (due to much smaller curvature radius).

Critical photon energy (analogous to (24)) reads

$$\varepsilon_{\text{sr}} = \frac{3}{2} \hbar \frac{eB}{m_e c} \gamma^2 \sin \psi. \quad (28)$$

For a monoenergetic injection function of particles (e^\pm -pairs in the context of this review) and their cooling due to SR the energy spectrum of SR spreads between a high-energy limit $\varepsilon_{\text{sr}}(\gamma_0)$ set by γ_0 of the injected (created) particles, and a low-energy turnover ε_{ct} determined by the condition $\gamma_\perp \sim 1$:

$$\varepsilon_{\text{ct}} \equiv \varepsilon_{\text{sr}}(\gamma = \gamma_\parallel) = \frac{3}{2} \hbar \frac{eB}{m_e c} \frac{1}{\sin \psi}. \quad (29)$$

The spectrum assumes a single power-law shape $f_\varepsilon(\varepsilon) \propto \varepsilon^{-1/2}$ (and accordingly $\varepsilon f_\varepsilon(\varepsilon) \propto \varepsilon^{+1/2}$) above the turnover. Below ε_{ct} , the spectrum f_ε changes its slope, asymptotically reaching $\propto \varepsilon^{+2}$. It is built up by contributions from low-energy tails emitted by particles with $\gamma_\perp \gg 1$, and each low-energy tail is assumed to cut off at local gyrofrequency, which in the reference frame comoving with the center of gyration is $\omega_B = \frac{eB}{m_e c \gamma_\perp}$.

The spectrum of SR calculated with Monte-Carlo method to model the Vela pulsar is shown in Fig.5 as a dashed line. The low-energy part of the SR spectrum at ε_{ct} seems to be essential for reproducing an interpolation between the RXTE and the OSSE data.

6.4 Magnetic Inverse Compton Scattering

Consider an electron with a Lorentz factor γ moving along a magnetic field line \mathbf{B} and a photon of energy $\varepsilon = \epsilon m c^2$ moving at angle $\arccos \mu$ to the field line. In the reference frame comoving with the electron (primed symbols) the counterpart of the free-space Compton formula, due to energy-momentum conservation appropriate for collisions with the electron at the ground Landau level both in the initial and final state, reads

$$\begin{aligned} \epsilon'_s = (1 - \mu_s'^2)^{-1} & \left\{ 1 + \epsilon'(1 - \mu' \mu'_s) + \right. \\ & \left. - \left[1 + 2\epsilon' \mu'_s (\mu'_s - \mu') + \epsilon'^2 (\mu'_s - \mu')^2 \right]^{1/2} \right\} \end{aligned} \quad (30)$$

where $\epsilon' = \epsilon \gamma (1 - \beta \mu)$ [41], and symbols with no subscript and with the subscript 's' refer to the state before the scattering and after the scattering, respectively. A longitudinal momentum of the electron in the electron rest frame changes due to recoil from zero to $(\epsilon' \mu' - \epsilon'_s \mu'_s) m c$.

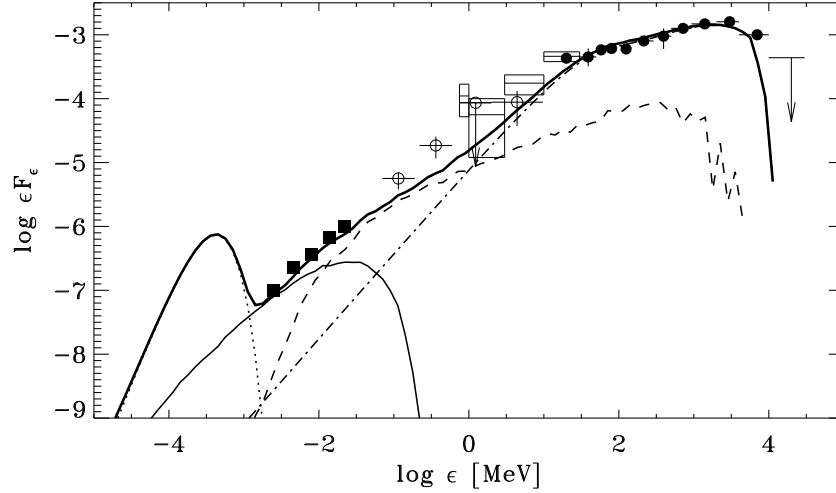


Fig. 5. The model energy spectrum calculated by [30] to reproduce the spectral features of the Vela pulsar ($P = 89$ ms, $B_s = 6 \times 10^{12}$ G). The accelerator is located at $h_0 = 3R_s$ above the surface (see Sect.6). The broad-band spectrum consists of four components due to: curvature radiation of primary electrons (dot-dashed), synchrotron radiation of secondary e^\pm -pairs (dashed), inverse Compton scattering of surface X-ray photons on the e^\pm -pairs (thin solid) and the blackbody surface emission (dotted). The surface temperature $T_s = 1.26 \times 10^6$ K was assumed. Total spectrum is given by a thick solid line. Phase-averaged data points for Vela from different satellite experiments are indicated. Filled squares – RXTE [71]; open circles – OSSE [70]; open squares – COMPTEL [68]; filled circles plus upper limit just above 10 GeV – EGRET [77]. Vertical axis is in log of $\text{MeV cm}^{-2} \text{s}^{-1}$ units.

The polarization-averaged relativistic magnetic cross section in the Thomson regime may be approximated with a nonrelativistic formula [28]:

$$\sigma = \frac{\sigma_T}{2} \left(1 - \mu'^2 + (1 + \mu'^2) \left[g_1 + \frac{g_2 - g_1}{2} \right] \right) \quad (31)$$

where σ_T is the Thomson cross section, and g_1 and g_2 are given by

$$g_1(u) = \frac{u^2}{(u+1)^2}, \quad g_2(u) = \frac{u^2}{(u-1)^2 + a^2} \quad (32)$$

where $u \equiv \epsilon'/\epsilon_B$, $a \equiv 2\alpha\epsilon_B/3$, $\epsilon_B \equiv \hbar eB/m^2c^3$ and α is a fine-structure constant. The resonance condition for the scattering is therefore the cyclotron resonance $\epsilon' = \epsilon_B$. The factor a represents a ‘natural’ broadening of the resonance due to finite lifetime at the excited Landau level.

In the Klein-Nishina regime ($\epsilon' > 1$) the relativistic magnetic cross section for the $|\mu'| \approx 1$ case becomes better approximated with the well known Klein-Nishina relativistic nonmagnetic total cross section σ_{KN} [25] [28].

The rate \mathcal{R} of scatterings subject by an electron moving across the field of soft photons, measured in the lab frame is

$$\mathcal{R} = c \int d\Omega \int d\epsilon \sigma \left(\frac{dn_{\text{ph}}}{d\epsilon d\Omega} \right) (1 - \beta\mu) \quad (33)$$

where $\Omega = d\mu d\phi$ is the total solid angle subtended by the source of soft photons, $\mu = \cos\theta$, σ is a total cross section for the process, and $dn_{\text{ph}}/d\epsilon/d\Omega$ is the local density of the soft photons.

The properties of the field of soft photons are usually simplified by taking $dn_{\text{ph}}/d\epsilon/d\Omega$ as for the blackbody radiation. This simplification should be taken with care since magnetised atmospheres of neutron stars introduce strong anisotropy as well as spectral distortions to the outgoing radiation [58]. Effectively it means that the ICS effects obtained with this simplification are just upper limits to the actual effects.

To estimate electron cooling rate $\dot{\gamma}_{\text{ICS}}$ due to the ICS the differential form of (31) is necessary:

$$\begin{aligned} \frac{d\sigma}{d\Omega'_s} = \frac{3\sigma_T}{16\pi} & \left[(1 - \mu'^2)(1 - \mu_s'^2) + \right. \\ & \left. + \frac{1}{4} (1 + \mu'^2)(1 + \mu_s'^2)(g_1 + g_2) \right] \end{aligned} \quad (34)$$

(eg. [26]), where $d\Omega'_s = d\phi'_s d\mu'_s$ is an increment of solid angle into which outgoing photons with energy ϵ'_s in the electron rest frame are directed. The mean electron energy loss rate then reads

$$\begin{aligned} \dot{\gamma}_{\text{ICS}} = -c \int d\epsilon \int d\Omega & \left(\frac{dn_{\text{ph}}}{d\epsilon d\Omega} \right) (1 - \beta\mu) \times \\ & \times \int d\Omega'_s \left(\frac{d\sigma}{d\Omega'_s} \right) (\epsilon_s - \epsilon) \end{aligned} \quad (35)$$

where $\epsilon_s = \epsilon'_s \gamma (1 + \beta\mu'_s)$ is the scattered photon energy in the lab frame (e.g.[28]).

The spectrum of magnetic ICS calculated numerically to model the Vela pulsar is shown in Fig.5 with thin solid line. The blackbody soft photons originating at the stellar surface (dotted line) are upscattered by secondary e^\pm -pairs at the expense of their “longitudinal” energy $\gamma_{\parallel} mc^2$, assumed to remain unchanged during the burst of synchrotron emission. Without the ICS component due to the e^\pm -pairs the RXTE data for the Vela pulsar would be difficult to reproduce within the model. It is worth to note, that the magnetic ICS component due to primary electrons (not shown in Fig.5) is energetically insignificant comparing to the CR component because the case of strong accelerating field was used in this particular model.

6.5 Photon splitting

Photon splitting into two photons in the presence of magnetic field B is a third-order QED process with no energy threshold [2]. The attenuation coefficient, after averaging over the polarization states, reads [38]

$$T_{\text{split}}(\epsilon) \approx \frac{\alpha^3}{10\pi^2} \frac{1}{\lambda_c} \left(\frac{19}{315}\right)^2 \left(\frac{B \sin \theta_{\text{kB}}}{B_{\text{crit}}}\right)^6 \epsilon^5 \text{ cm}^{-1}, \quad (36)$$

(provided B does not exceed B_{crit} substantially) where α is a fine structure constant, ϵ is the photon energy in units of mc^2 , θ_{kB} is the angle between photon momentum vector and the local magnetic field. The process, therefore, strongly depends on magnetic field strength B .

Photon splitting has attracted substantial interest in recent years due to the discovery of neutron stars with supercritical magnetic fields (i.e. magnetars; see Fig.6) [50]. It has been analysed in details by [38] and incorporated in a Monte Carlo code tracing the propagation of electromagnetic cascades in the magnetospheres of high- B pulsars. The effect was found to explain satisfactorily the unusual cut-off observed in the gamma-ray spectrum of B1509-58 (see Sect.3). Generally, it becomes competitive to the magnetic pair creation for dipolar magnetospheres with $B_s \gtrsim 0.3B_{\text{crit}}$ [38]. The degradation of photon energy in the course of splitting inhibits also any development electromagnetic cascades. In consequence, high- B RPP should not emit coherent radio emission. Indeed, there exists a high- B region in the $P - \dot{P}$ diagram (Figs.1,6) void of radiopulsars. Even though recently discovered (during The Parkes Multibeam Pulsar survey) two high- B radiopulsars [17] are located above the limiting line derived by [6], the general argument for magnetars expected to be radio-quiet RPP remains valid [86].

7 RPP as sources of UHECR generated beyond the light cylinder

The hypothesis that cosmic ray events above $\sim 5 \times 10^{19}$ eV, i.e. above the GZK cutoff, are due to charged particles accelerated by strongly magnetised neutron stars is being kept under consideration [14][56][11] apparently for two reasons. First, within Down–Top scenarios which rely on conventional physics a list of classes of objects satisfying a necessary condition to generate such cosmic rays is rather short according to the appealing Hillas diagram [42]. Second, no compelling breakthrough has been achieved in studying other candidates in this context, though central engines of AGN or jets extending from Fanaroff-Riley II radio galaxies [12] take rather high positions in the list [57].

In the case of neutron stars the most promising and natural reservoir of required energy is the rotational energy of the stars, a point reiterated on numerous occasions, e.g.[79], and assumed in most models. There are three

fundamental features discriminating the models:

- 1) the site of acceleration with respect to the neutron star,
- 2) the mechanism allowing to tap the rotational energy by charged particles,
- 3) the nature and origin of the charged particles subject to acceleration.

Simple but sounding arguments supported by observed HE-radiation properties of RPP make the first point rather clear: the process of particle acceleration should take place beyond the light cylinder. Potential advantage of this choice over acceleration process within the light cylinder is twofold. First, full potential drop across open field lines $\Delta\Phi_{\text{pc}}$ (14) is available, at least in principle, for particles outside the light cylinder, whereas the capability of an accelerator inside the magnetosphere is severely constrained by copious formation of electron-positron pairs which short out the electric field \mathcal{E}_{\parallel} easily, i.e. $\Delta\Phi_{\parallel} < \Delta\Phi_{\text{pc}}$. Second, unlike inside the magnetosphere, the acceleration of charged particles is not limited by any radiation losses – a point especially important in the context of UHECR. Therefore, a particle of charge Ze reaches then maximal possible energy

$$E_{\text{max}} \approx Ze \Delta\Phi_{\text{pc}} = 6 \times 10^{19} Z B_{13} P_{\text{ms}}^{-2} \text{eV}, \quad (37)$$

(where $B_{13} \equiv B_s/10^{13}\text{G}$) which is substantially higher than the energy E_p which can be attained in the accelerating field of either the polar gap or outer gap: $E_p \ll Ze \Delta\Phi_{\parallel} < E_{\text{max}}$.

The idea of UHECR events due to an accelerator or a converter of the rotational energy into kinetic energy of particles, located beyond the light cylinder has been pursued recently in a couple of diametrically different models. Historically the first model considered the fate of charged particles injected into the plerionic nebula powered by a shocked relativistic wind from a central pulsar [10] [48]. This model was motivated by the theoretical analysis of magnetohydrodynamics within the Crab Nebula [60] [45] [21]. The acceleration was proposed to occur in the electric field of the shocked wind. A simple structure of the electric field was derived as induced by the relativistic radial wind crossing a toroidal magnetic field (which originates inside the light cylinder, at the stellar surface) with assumed radial and angular dependence after [60] and [21]. Charged particles entering the nebula are subject to the $\mathcal{E} \times \mathbf{B}$ drift as well as to the ∇B drift (due to strong inhomogeneity in \mathbf{B}) along various paths, and may gain energy at the expense of \mathcal{E} before exiting. Since the electric field is potential here, the net change in the particle energy does not depend on the path but solely on the points of entry and exit. In particular, the maximal gain ΔE of energy is due to potential difference between the pole (fixed by the rotation axis of the pulsar) and the equator (cf. (3) in [48]), and actually it equals to E_{max} given by (37). In order for the particle to penetrate the nebula from outside it should be already highly relativistic, with $E_{\text{init}} \sim 10^{15}\text{eV}$, presumably pre-accelerated by diffusive acceleration at the outer shock where the supernova remnant meets the interstellar medium. Otherwise the Larmor radius of the particle is too small for the ∇B inward drift at the pole (the case relevant for one combination of signs of \mathbf{B}

and Ze) to counter the $\boldsymbol{\mathcal{E}} \times \boldsymbol{B}$ outward drift. Though very attractive, the model is unable to make any strong predictions about spectral properties of its UHECR without reliable assumptions about spatial distribution and directional properties of the pre-accelerated particles.

All other models make use of charged particles, either protons or iron nuclei, coming from within the light cylinder i.e. supplied by a neutron star itself.

A recently proposed phenomenological model of UHECR within the Galaxy incorporates iron Fe^{26} nuclei ($Z = 26 Z_{26}$) accelerated in a relativistic MHD wind flowing out of very young, rapidly rotating highly magnetised neutron stars [15]. The number of nuclei crossing the light cylinder per unit time is taken equal to the Goldreich–Julian rate estimated at the polar cap

$$\dot{N}(\text{Fe}^{26}) \approx \dot{N}_{\text{GJ}} = A_{\text{pc}} \frac{\varrho_{\text{GJ}}}{Ze c}, \quad (38)$$

where $A_{\text{pc}} \simeq \pi R_{\text{s}}^3 R_{\text{lc}}^{-1}$ and ϱ_{GJ} is defined in (18). It is also assumed that electron-positron pairs formed within the magnetosphere do not dominate the flow in terms of the rest mass. This is a reasonable assumption because otherwise the number of created e^\pm pairs per nucleus would have to exceed $m_{\text{Fe}}/2m_e \approx 5 \times 10^4$ which is unlikely in very strong magnetic fields $B_{\text{s}} > 10^{13}\text{G}$ due to photon-splitting effects [38]. A key postulate of the model is that transfer of a sizeable fraction ($\xi \lesssim 1$) of the spindown luminosity occurs just beyond the light cylinder into the kinetic energy flux of the ions. At the light cylinder, however, the spindown luminosity (i.e. the rotational energy loss rate) is usually thought to be dominated by the Poynting flux (of low-frequency electromagnetic waves). In terms of the so called magnetization parameter σ which is defined as the ratio of the Poynting flux to the the particle kinetic energy flux [60] [21] it means that – whatever the reason – σ does not remain constant in the wind: $\sigma \gg 1$ at the light cylinder converts further out to $\sigma \ll 1$, i.e. the wind must depart from an ideal MHD flow case. This picture is motivated again by the wind models for the Crab Nebula (e.g. [31] [45], see also [65] for calorimetric properties of the Crab Nebula, and [3] for an account of the problem of the coupling of RPP to plerionic nebulae). No consensus about likely mechanisms responsible for the dissipation of the Poynting flux has been reached so far, though several models have been proposed (e.g. [21] [9]). For a single average iron nucleus the postulated conversion means acceleration up to

$$E_{\text{UHECR}} \approx L_{\text{sd}}/\dot{N}(\text{Fe}^{26}) \approx Ze \Delta\Phi_{\text{pc}} \approx 10^{21} Z_{26} B_{13} P_{\text{ms}}^{-2} \text{eV}, \quad (39)$$

where (38) was used. Similarly as in the previous model, the energy gain is in fact directly related to the full potential drop $\Delta\Phi_{\text{pc}}$ across open field lines. For a fully ionized iron ($Z_{26} = 1$) to reach $E_{\text{UHECR}} = 10^{20}\text{eV}$ the pulsar would have to be fastly spinning and highly magnetised (for example $P = 0.001\text{s}$ and $B_{\text{s}} = 10^{12}\text{G}$). According to [15], the region in the $P - B_{\text{s}}$ space occupied

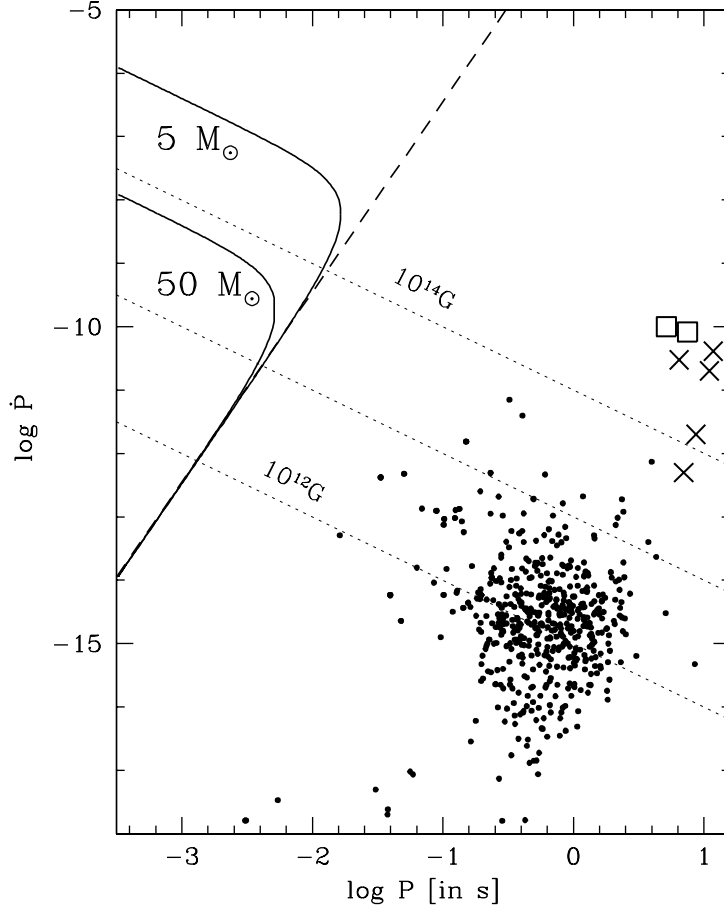


Fig. 6. The high- B_s part of the $P - \dot{P}$ diagram (see Fig.1). Dashed line indicates the full potential drop $\Delta\Phi_{pc}$ across open field lines equal to $\frac{1}{26} \times 10^{20}$ V. The allowed region in the model of [56] to accelerate a fully ionized atom of iron ($Z = 26$) to the energy of 10^{20} eV and let it traverse the pre-supernova envelope without spallation effects lies to the left of two solid lines which are drawn for two values of the mass of the envelope: $5M_\odot$ and $50M_\odot$. A group of magnetars, clustered around $P \sim 10$ s is also indicated after [50] although their X-ray activity is not driven by rotational energy losses (i.e. they do not belong to the class of RPP) but rather involves accretion or the decay of strong magnetic field. Open squares and crosses denote SGR and AXP, respectively.

by pulsars satisfying the requirement $E_{\text{UHECR}} = 10^{20}\text{eV}$ is actually even more constrained than (39) suggests. The magnetic field of the pulsar should not be too strong to make sure that the characteristic time scale of spin-down τ is not too short allowing thus the expanding pre-supernova envelope of mass M_{env} to disperse and become transparent so the iron nuclei would escape it without significant spallation. For M_{env} equal $5M_{\odot}$ and $50M_{\odot}$ the magnetic field B_s should not exceed $\sim 6 \times 10^{13}\text{G}$ and $\sim 6 \times 10^{14}\text{G}$, respectively (see Fig.6). A factor not discussed in [15] but likely to further constrain the allowed region in the $B_s - P$ space in order to make the model work is a poorly known cohesive or binding energy $\Delta\varepsilon_c$ of iron on the high- B_s neutron star surface. For $B_s > 10^{13}\text{G}$ $\Delta\varepsilon_c$ may exceed 5 keV [1]. Thermionic emission of iron nuclei is then impossible unless the surface temperature exceeds $\sim 3 \times 10^6\text{K}$ within the first $\sim 10^8\text{s}$ [54] after the neutron star formation which is a characteristic time scale mediated by the neutron star's spin-down when the energy E_{max} drops below a required CR energy $\sim 10^{20}\text{eV}$, and the expansion of the envelope during which it becomes transparent to the Fe nuclei. The only supply of iron nuclei may then occur via field emission. Making modest assumptions about the distribution of rapidly rotating neutron stars, the rates of their birth and – most importantly – the efficiency rate for acceleration of the particles at the light cylinder, an expected flux of these particles on Earth is compared to the data. The calculated particle spectrum above $5 \times 10^{19}\text{eV}$ is flat, $N_{\text{Fe}} \propto E^{-\gamma}$ with $\gamma = 1$, and therefore should be visible as a distinct component in the CR spectrum, which is much steeper below $5 \times 10^{19}\text{eV}$ with the power-law index $\gamma \approx 3$. However, the number of events above $5 \times 10^{19}\text{eV}$ detected so far is insufficient for describing them in terms of spectral features [22].

For a pulsar capable of producing UHECR as in [15], a natural continuation – as it slows down its rotation and becomes a Crab-like object – would be to generate CR particles of lower energy. Hadronic model proposed by [8] seems to be relevant in this context, since it describes the fate of iron nuclei extracted from the pulsar surface and then subject to acceleration. However, a different acceleration site is considered here: the nuclei are assumed to accelerate within the light cylinder, in outer gaps of [20] (i.e. the type of accelerator not addressed in this review). Once the nuclei achieve high energy ($\gamma_{\text{Fe}} > 10^5$) they disintegrate in the field of soft photons present in the outer gap. Relativistic neutrons extracted in this way decay into protons either inside or outside the surrounding nebula. In the first case, these relativistic protons interact with nebular material via pp processes giving rise to VHE photons and neutrinos. In the second case, cosmic ray protons peaking at $\sim 10^{15} - 10^{16}\text{eV}$ (close to the knee in the CR spectrum) are produced.

A distinct model of UHECR particles above the GZK cutoff has been recently proposed [36]. It postulates that UHECR are protons accelerated in reconnection sites above the magnetospheres of very young pulsars formed by accretion-induced collapse of white dwarves (AIC). Promising candidates

would occupy roughly the same region of the $P - \dot{P}$ space as indicated for the model of [15] (the less massive envelope case) in Fig.6. Since the estimated rate of AIC events per galaxy is too low to rely just on our Galaxy, the contribution of all galaxies within the distance of about 50 Mpc is necessary to reach the observed rate of UHECR events.

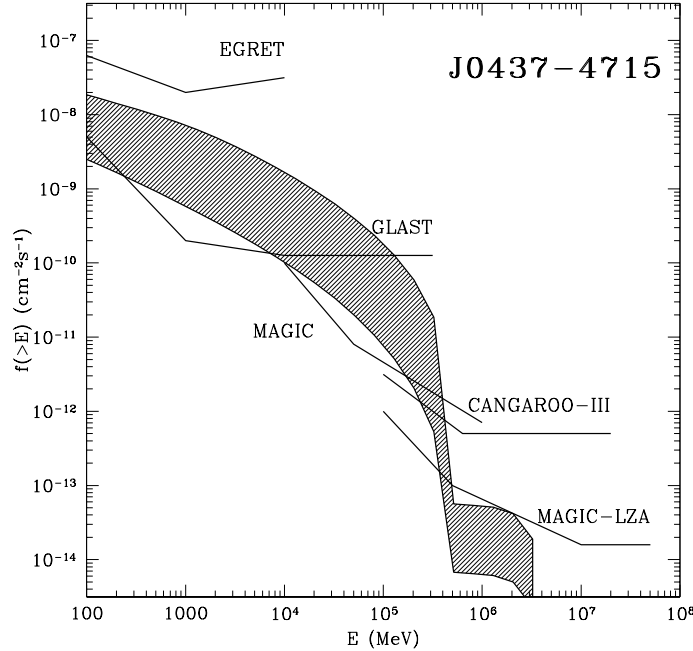


Fig. 7. Cumulative spectral flux of photons expected for the millisecond pulsar J0437-4715 at a distance of 140 pc according to [16]. The shaded region shows the range of flux levels due to uncertainty in the maximal energy of primary electrons. The main part of the spectrum is due to curvature radiation of the electrons. The additional feature reaching the VHE domain is due to inverse Compton scattering of soft photons from the surface with the temperature $4 \times 10^5 \text{K}$. Sensitivities of EGRET as well as three major HE and VHE experiments of the future are also indicated. MAGIC-LZA denotes sensitivity of MAGIC in its Large Zenith Angle mode.

8 Concluding remarks

High energy astrophysics of neutron stars received an impressive boost from two major satellite missions of the past – ROSAT and CGRO, backed by

still ongoing experiments – ASCA, BeppoSAX and RXTE. Theoretical astrophysics of RPP was confronted with– and surprised by an unprecedented variety of spectral and temporal properties among the detected sources. Another unexpected challenge came from radio-astronomy, due to superb performance of The Parkes Multibeam Pulsar Survey, with recent discoveries of radiopulsars, with extremely high magnetic fields in two cases and an extremely long spin period in another case. Numerous modifications (both, minor and major) to the existing models of magnetospheric activity were invented to accommodate at least some of these properties. Several predictions have been presented which would hopefully discriminate between those models. It will be impossible, however, to verify those predictions without achieving higher sensitivities and exploring new energy domains.

A break-through in understanding rotation powered pulsars and their pleurionic environments should then come from HE/VHE astronomy of the near future, with its planned satellite and ground-based experiments. Expected sensitivity and energy range for some of them is presented in Fig.7 along with a predicted flux from a nearby millisecond pulsar, overlaid for the sake of comparison. The satellite experiment GLAST [44] will be superior to its predecessor – EGRET on board CGRO – in two aspects. First, its sensitivity at 10 GeV will be three orders of magnitude better than that of EGRET. Second, it will reach energy of 300 GeV, closing thus for the first time a wide gap in energy between ground-based and satellite experiments. The MAGIC Telescope [13] – a 17 m diameter Imaging Air Cherenkov Telescope (IACT) – is expected to operate with sensitivity about three orders of magnitude higher at 10 GeV than EGRET. Its advanced technology will make possible to cover energy range between 10 GeV and 1 TeV, and to reach ~ 50 TeV in the Large Zenith Angle mode. Energy ranges of GLAST and MAGIC will overlap over more than one decade in energy. Another proposed IACT, VERITAS [82], will be an array of seven 10 m telescopes, covering energy range from 50 GeV to 50 TeV with planned sensitivity at 1 TeV about ten times better than MAGIC.

Acknowledgments

I am grateful to J. Arons, W. Bednarek, T. Bulik, K.S. Cheng, J. Dyks, E.M. de Gouveia Dal Pino, M. Gros, P. Haensel, O.C. de Jager, A.V. Olinto, S. Shibata, T.C. Weekes, and B. Zhang for sharing with me their views and opinions on issues addressed in this review. Financial support by KBN grant 2P03D02117 is acknowledged.

References

1. A.M. Abrahams, S.L. Shapiro: *ApJ* **374**, 652 (1991) V.V. Usov, D.B. Melrose: *Aus.J.Phys.* **48**, 571 (1995)

2. S.L. Adler: *Ann.Phys.* **67**, 599 (1971)
3. J. Arons: *Mem. Soc. Ast. Ital.* **69**, 989, (1998)
4. J. Arons, E.T. Scharlemann: *ApJ* **231**, 854(1979)
5. J. Arons: ‘Pulsar Death at an Advanced Age’. In: *IAU Coll. 177, Pulsar Astronomy – 2000 and beyond* ed. M. Kramer, N. Wex, R. Wielebinski (ASP Conference Series **202**: 2000) pp.449-454
6. M.G. Baring, A.K. Harding: *ApJ* **507**, L55 (1998)
7. W. Becker, J. Trümper: *A&A* **326**, 682 (1997) W. Becker, J. Trümper: *A&A* **341** 803 (1999)
8. W. Bednarek, R.J. Protheroe: *Phys.Rev.Lett.* **79**, 2616 (1997)
9. M.C. Begelman, Z.-Y. Li: *ApJ* **426**, 269 (1994)
10. A.R. Bell: *MNRAS* **257**, 493 (1992)
A.R. Bell, S.G. Lucek: *MNRAS* **283**, 1083 (1996)
11. P. Bhattacharjee, G. Sigl: *Phys.Rep.* **327**, 109 (2000)
12. P.L. Biermann: *Phys.Rev. D* **51**, 3450 (1995)
13. O. Blanch, G. Blanchot, M. Bosman, et al.: ‘The MAGIC telescope’, Letter of Intent (1998)
14. R.D. Blandford: preprint, astro-ph/9906026, (1999)
15. P. Blasi, R.I. Epstein, A.V. Olinto: *ApJ* **533**, L123 (2000)
16. T. Bulik, B. Rudak, J. Dyks: *MNRAS* **317**, 97 (2000)
17. F. Camilo, et al.: *ApJ* **541**, 367 (2000)
18. K. Chen, M. Ruderman: *ApJ* **402**, 264 (1993)
19. K.S. Cheng, L. Zhang: *Fundamentals of Cosmic Physics* **20**, 177 (1999)
K.S. Cheng, L. Zhang: *ApJ* **515**, 337 (1999) L. Zhang, K.S. Cheng: *ApJ* **487**, 370 (1997)
20. K.S. Cheng, C. Ho, M.A. Ruderman: *ApJ* **300**, 500 (1986) K.S. Cheng, C. Ho, M.A. Ruderman: *ApJ* **300**, 522 (1986)
21. F.V. Coroniti: *ApJ* **349**, 538 (1990)
22. J.W. Cronin: *Rev. Mod. Phys.* **71**, S165 (1999)
23. J.K. Daugherty, A.K. Harding: *ApJ* **252**, 337 (1982)
24. J.K. Daugherty, A.K. Harding: *ApJ* **273**, 761 (1983)
25. J.K. Daugherty, A.K. Harding: *ApJ* **309**, 362(1986)
26. J.K. Daugherty, A.K. Harding: *ApJ* **336**, 861(1989)
27. J.K. Daugherty, A.K. Harding: *ApJ* **429**, 325 (1994) S.J. Sturmer, C.D. Dermer: *ApJ* **420**, L79 (1994) A.K. Harding, A.G. Muslimov: *ApJ* **500**, 862 (1998)
28. C.D. Dermer: *ApJ* **360**, 197 (1990)
29. J. Dyks, B. Rudak: *A&A* **362**, 1004 (2000)
30. J. Dyks, B. Rudak, T. Bulik: *Proc. of the 4th INTEGRAL Workshop*, astro-ph/0010301, (2000)
31. R.T. Emmering, R.A. Chevalier: *ApJ* **321**, 334 (1987)
32. T. Erber: *Rev.Mod.Phys.* **38**, 626 (1966)
33. J.M. Fierro et al.: *ApJ* **447**, 807 (1995)
34. P. Goldreich, W.H. Julian: *ApJ* **157**, 869 (1969)
35. E.V. Gotthelf, G. Vasisht, M. Boylan-Kolchin, K. Torii: *ApJ* **542L**, 37 (2000)
36. E.M. de Gouveia Dal Pino, A. Lazarian: *ApJ* **535**, L31 (2000)
37. J.P. Halpern, F.Y.-H. Wang: *ApJ* **477**, 905 (1997)
38. A.K. Harding, M.G. Baring, P.L. Gonthier: *ApJ* **476**, 246 (1997) M.G. Baring, A.K. Harding: to appear in *ApJ* **547**, February 1 issue (2001)

39. A.K. Harding, I. Contopoulos, D. Kazanas: ApJ **525**, L125 (1999)
40. A.K. Harding, A.G. Muslimov: ApJ **508**, 328 (1998)
41. H. Herold: Phys.Rev.D **19**, 2868 (1979)
42. A.M. Hillas: A&A **22**, 425 (1984)
43. W.N. Johnson et al.: ApJS **86**, 693 (1993) V. Schönfelder et al.: ApJS **86**, 657 (1993) D.J. Thompson et al.: ApJS **86**, 629 (1993)
44. T. Kamae, T. Ohsugi, D.J. Thompson, K. Watanabe: Adv.Sp.Res. **25**, 905 (2000)
45. C.F. Kennel, F.V. Coroniti: ApJ **283**, 694 (1984) C.F. Kennel, F.V. Coroniti: ApJ **283**, 710 (1984)
46. L. Kuiper et al.: A&A **351**, 119 (1999)
47. L. Kuiper et al.: A&A **359**, 615 (2000)
48. S.G. Lucek, A.R. Bell: MNRAS **268**, 581 (1994)
49. F.E. Marshall, E.V. Gotthelf, W. Zhang, J. Middleditch, Q.D. Wang: ApJ **499L** 179 (1998)
50. S. Mereghetti: NATO ASI “The Neutron Star – Black Hole Connection” (1999)
51. F.C. Michel: *Theory of Neutron Star Magnetospheres*. (The University of Chicago Press, Chicago 1991) P. Mészáros: *High-Energy Radiation from Magnetized Neutron Stars*. (The University of Chicago Press, Chicago 1992)
52. A.G. Muslimov, A.I. Tsygan: MNRAS **255**, 61 (1992)
53. H.I. Nel et al.: ApJ **465**, 898 (1996)
54. K. Nomoto, S. Tsuruta: ApJ **312**, 711 (1987) J.M. Lattimer, K.A. Van Riper, M. Prakash, M. Prakash: ApJ **425**, 802 (1994)
55. H. Ögelman: ‘X-Ray Observations of Cooling Neutron Stars’. In: *NATO ASI, The Lives of Neutron Stars* ed. M.A. Alpar, Ü. Kızıloğlu, J. van Paradijs (Dordrecht: Kluwer 1995) pp.101-120
56. A.V. Olinto: preprint submitted to Elsevier Preprint, astro-ph/0002006, (2000)
57. R. Ong: astro-ph/0003014 (2000)
58. G.G. Pavlov, Y.A. Shibano, J. Ventura, V.E. Zavlin: A&A **289**, 837(1994)
59. A. Possenti, S. Mereghetti, M. Colpi: A&A **313**, 565 (1996)
60. M.J. Rees, J.E. Gunn: MNRAS **167**, 1 (1974)
61. B. Rudak, J. Dyks: MNRAS **295**, 337 (1998)
62. B. Rudak, J. Dyks: MNRAS **303**, 477 (1999)
63. Y. Saito et al.: ApJ **477** L37 (1997) Y. Saito, N. Kawai, T. Kamae, S. Shibata: ‘Search for X-ray pulsations from Rotation-Powered Pulsars with ASCA’. In: *Neutron Stars and Pulsars: Thirty Years after the Discovery* ed. N. Shibasaki, N. Kawai, S. Shibata et al. (Universal Academy Press: Tokyo 1998) pp.295-298
64. T. Sako, Y. Matsubara, Y. Muraki et al.: ApJ **537**, 422 (2000)
65. S. Shibata, N. Kawai, K. Tamura: ‘Pulsar Nebulae as Calorimeters’. In: *Neutron Stars and Pulsars: Thirty Years after the Discovery* ed. N. Shibasaki, N. Kawai, S. Shibata et al. (Universal Academy Press: Tokyo 1998) pp.457-464
66. P. Slane: ApJ **437**, 458 (1994)
67. P. Slane, N. Lloyd: ApJ **452L**, 115 (1995)
68. V. Schönfelder et al.: A&AS **143**, 145 (2000)
69. P.C. Schroeder, M.P. Ulmer, S.M. Matz et al.: ApJ **450**, 784 (1995)

70. M.S. Strickman et al.: ApJ **460**, 735 (1996)
71. M.S. Strickman, A.K. Harding, O.C. de Jager: ApJ **524**, 373 (1999)
72. S.J. Sturmer: ApJ **446**, 292(1995)
73. S.J. Sturmer, C.D. Dermer, F.C. Michel: ApJ **445** 736 (1995) C.D. Dermer, S.J. Sturmer: ApJ **420**, L75 (1994)
74. P.A. Sturrock: ApJ **164**, 529, (1971)
75. M. Takahashi et al.: ‘Detection of Pulsed X-ray Emission from The Fastest Millisecond Pulsar PSR B1937+21 with ASCA’. In: *IAU Coll. 177, Pulsar Astronomy – 2000 and beyond* ed. M. Kramer, N. Wex, R. Wielebinski (ASP Conference Series **202**: 2000) pp.353-354
76. J.H. Taylor, R.N. Manchester, A.G. Lyne, F. Camilo: ‘The Princeton Pulsar Database’ (<http://pulsar.princeton.edu>) (1995) J.H. Taylor, R.N. Manchester, A.G. Lyne: ApJS **88**, 529 (1993)
77. D.J. Thompson, A.K. Harding, W. Hermsen, M.P. Ulmer: ‘Gamma-Ray Pulsars: the Compton Observatory Contribution to the Study of Isolated Neutron Stars’. In: *Fourth Compton Symposium* ed. by C.D. Dermer, M.S. Strickman, J.D. Kurfess (New York: AIP 1997) 410
78. D.J. Thompson et al.: ApJ **516**, 297, (1999)
79. A. Venkatesan, M.C. Miller, A.V. Olinto: ApJ **484**, 323 (1997)
80. H. Völk, HEGRA Collaboration: ‘HEGRA Observations of Galactic Sources’. In: *GeV-TeV Gamma Ray Astrophysics Workshop : towards a major atmospheric Cherenkov detector VI* ed. B.L. Dingus, M.H. Salamon, D.B. Kieda: AIP Conference Proceedings, Vol. 515., p.197 (New York: AIP 2000) F. Aharonian et al.: A&A **346**, 913 (1999) R.W. Lessard et al.: ApJ **531L**, 942 (2000)
81. T.C. Weekes: ‘VHE Astronomy Before the New Millennium’. In: *GeV-TeV Gamma Ray Astrophysics Workshop : towards a major atmospheric Cherenkov detector VI* ed. B.L. Dingus, M.H. Salamon, D.B. Kieda: AIP Conference Proceedings, Vol. 515., p.3 (New York: AIP 2000) M. Catanese, T.C. Weekes: PASP **111**, 1193 (1999)
82. T.C. Weekes, S.M. Bradbury, I.H. Bond et al.: ‘The Very Energetic Radiation Imaging Telescope Array System (VERITAS)’, preprint (2000)
83. X.Y. Xia, G.J. Qiao, X.J. Wu, Y.Q. Hou: A&A **152**, 93 (1985) H.K. Chang: A&A **301**, 456 (1995)
84. M.D. Young, R.N. Manchester, S. Johnston: Nature **400**, 848 (1999)
85. B. Zhang, A.K. Harding: ApJ **532**, 1150 (2000)
86. B. Zhang, A.K. Harding: ApJ **535**, L51 (2000)